# Microstructure and mechanical properties of laser welded and post-weld heat-treated K439B superalloy

Zheng LI[1,2], Zhen-lin ZHANG[3], Ai-ping WU[1,2,4], Ming-jun ZHANG[5],
Ju KANG[6], Qu LIU[1,2], Yue ZHAO[1,2], Jing-yang CHEN[5]

1. Department of Mechanical Engineering, Tsinghua University, Beijing 100084, China;
2. Key Laboratory for Advanced Materials Processing Technology, Ministry of Education, Tsinghua University,
Beijing 100084, China;
3. School of Materials Science and Engineering, Southwest Jiaotong University, Chengdu 610031, China;
4. State Key Laboratory of Tribology, Tsinghua University, Beijing 100084, China;
5. Science and Technology on Advanced High Temperature Structural Materials Laboratory,
Beijing Institute of Aeronautical Materials, Beijing 100095, China;
6. Beijing Higher Institution Engineering Research Center of Energy Engineering Advanced Joining Technology,
Beijing Institute of Petrochemical Technology, Beijing 102617, China

**Abstract:** Laser welding of the new nickel-based alloy K439B applied for engine turbine was carried out. The effects of post-welding heat treatment (PWHT) on the microstructure and mechanical properties of the joints were investigated. Semi-quantitative statistical results show that after PWHT, $\gamma'$ phases in the whole joint grow up, and the radii of the primary and secondary $\gamma'$ phases are about 25 and 150 nm, respectively. The results of mechanical properties show that PWHT improves the microhardness in the weld by about HV 100, and the critical resolved shear stress provided by $\gamma'$ phases increases from 4.8 to 92 MPa. The tensile strength and yield strength of the heat-treated joint are comparable to those of the base metal. The presence of a large amount of carbides is the reason for the preferential fracture of the base metal during the tensile process.

**Key words:** nickel-based superalloy; laser welding; $\gamma'$ phases; carbides; microstructure; mechanical properties

## 1 Introduction

K439B superalloy is a new $\gamma'$ precipitation-strengthened nickel-based superalloy with higher temperature bearing capacity designed to replace K4169 alloy [1]. The weldability evaluation of K439B and the research on the microstructure and properties of the joints are of great value in academic and engineering applications. Laser welding has the advantages of high energy density, low welding heat input, and low thermal impact on the base metal [2], which is one of the ideal technologies to obtain high-quality K439B alloy joints [3]. In welding solidification process, serious component segregation often occurs, which easily induces solidification crack, liquation crack and other hot cracks [4−7]. The sum of Al and Ti contents of K439B alloy is controlled below 5.5 wt.%, but K439B alloy also has a relatively high Ti/Al ratio. The calculation shows that the antiphase boundary energy (APB) energy in the (111) plane of $Ni_3Al$ is 181 $mJ/m^2$, and when Ti replaces Al, APB energy exceeds 600 $mJ/m^2$ [8].

Therefore, the high Ti/Al ratio improves the strength of nickel-based alloy [9,10]. However, the effect is that the high Ti/Al ratio will aggravate the lattice mismatch of $\gamma/\gamma'$ phase. LIU et al [11] found that compared with the sample with high Ti/Al ratio, the $\gamma'$ phases in the sample with low Ti/Al ratio can maintain the spherical morphology after long-term aging, and have higher thermal stability. The base metal with higher mismatches generates more strain in the welding pool and is susceptible to cracking [12]. The weldability of K439B alloy requires further evaluation. Another particle that affects nickel-based alloys much is carbide. The ratio of Nb/Ta in K439B alloy is quite low. For MC-type carbides, NbC is more stable than $TiTaC_2$ [13,14]. The MC-type carbides (more $TiTaC_2$) in K439B alloy are relatively easy to transform and refine in subsequent heat treatment, which is conducive to improving the room temperature strength and plasticity [15,16].

Pre-welding heat treatment can effectively promote element diffusion, improve composition uniformity and weldability of base metal [17,18]. ALBARRAN et al [19] found that appropriate heat treatment for IN 939 alloy could produce spherical $\gamma'$ phases with low degree of lattice misfit with $\gamma$ matrix and no obvious dislocation was formed, which ultimately reduced the generation of thermal cracks in HAZ. TAHERI et al [20] also found that the volume fraction of $\gamma'$ phases increased by 5% and the room temperature tensile strength increased from 476 to 488 MPa after homogenizing the alloy at 1200 °C for 2 h and then air cooling before welding. Simultaneously, post-welding heat treatment process of solution and aging is generally required after welding. XIE et al [21] conducted solution and aging treatment on the laser welded joints of K4750 alloy and found that the absence of 50 nm spherical $\gamma'$ phases caused by post-welding aging treatment resulted in an increase in microhardness of the fusion zone from HV 250 to HV 380.

The weldability, microstructure and properties of the welded joints of K439B nickel-based alloy are not well understood, which cannot provide sufficient guidance for the practical engineering requirement. Based on this situation, the laser welding of K439B is carried out, and the hot cracking sensibility of K439B is evaluated by fish-bone method. Then, the microstructure characteristics of the defect-free joint before and after heat treatment are analyzed and the microstructure evolution behavior of the joint is revealed. Finally, the K439B joint is evaluated in terms of microhardness and tensile properties at room temperature. The relationship between the microstructure and mechanical properties of laser welded joints is clarified.

## 2 Experimental

In the actual production process, K439B alloys are obtained by vacuum investment casting. The size of the welding plate was 110 mm × 60 mm × 2 mm (length × width × thickness). Figure 1 shows the microstructure of the alloy in the solution state. The chemical elements of K439B mainly include
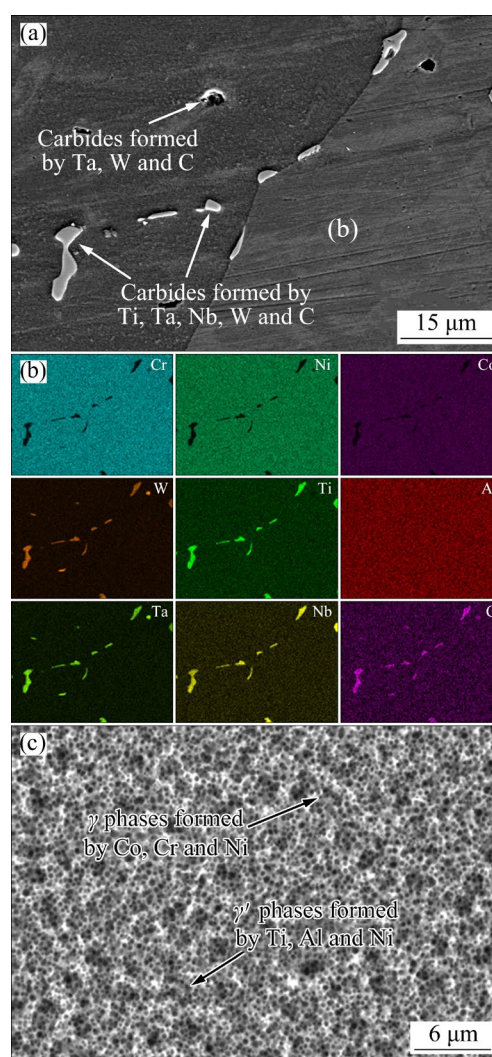


**Fig. 1** Microstructure and composition of phases in base metal after solution treatment: (a) Carbides; (b) EDS results of corresponding area; (c) $\gamma$ matrix and $\gamma'$ phases

Ni, Cr, Co, W, Al, Ti, Nb, Ta and C, and the total content of Ti and Al in K439B is controlled within 5.5 wt.%. Before welding, the alloy is treated with solution heat treatment, which can make the coarse $\gamma'$ phases and $\gamma-\gamma'$ eutectic dissolve into the $\gamma$ matrix, promote the diffusion of elements, reduce segregation, and improve the uniformity of composition [22].

The laser welding device is composed of a YLS−6000 fiber laser which outputs a continuous-wave laser and the welding device includes a KR60HA manipulator from the KUKA Company and a laser beam guided arm YW52 connected at the end. The parameters of laser welding are shown in Table 1. During butt welding without additional filler metal, the face and back of the alloy plate are protected by high-purity argon gas. After the welding is completed, the I-type welded plate is cooled to room temperature in the air.

**Table 1** Experimental parameters of laser welding process

| Parameter | Value or characteristic |
|---|---|
| Laser power/kW | 0.7−2.5 |
| Welding speed/(m·min$^{-1}$) | 1−2.5 |
| Defocusing distance/mm | 0 |
| Laser emitting mode | Continuous |

The hot cracking sensibility of K439B is evaluated by a fish-bone cracking test [23]. Fish-bone cracking test is a method to test the thermal cracking sensibility of alloys by base metal test plates with grooves of different lengths, which generate different maximum tensile stresses [24]. The K439B alloy with the size of 90 mm × 25 mm × 2 mm (length × width × thickness) is cut by wire electrical discharge with several notches of 1 mm in width and different depths, and the spacing between the adjacent cuts is 9 mm. Butt welding is carried out on two plates from $A$ with high constraint to $B$ with low constraint, as shown in Fig. 2. Five welds are obtained by laser butt welding with the parameter getting defect-free joints (In this paper, the parameters are laser power of 2.1 kW and welding speed of 1.5 m/min). The length of weld surface crack is observed and measured by the penetration flaw detection method. Alloy crack sensitivity ($C_l$) is defined by the formula: $C_l=L_l/L\times100\%$, where $L_l$ is the total length
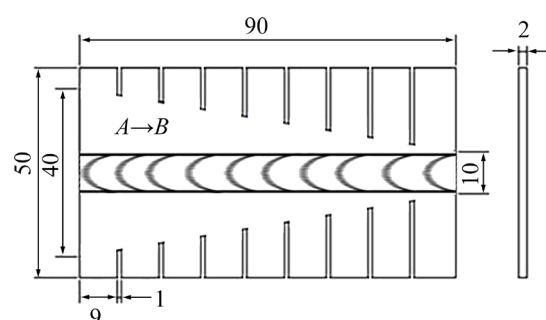


**Fig. 2** Size of specimens for fish-bone cracking test (unit: mm) [24]

of cracks on the face and back of every weld, and $L$ is the length of the weld, i.e. 90 mm [25].

The post-weld heat treatment (PWHT) process of solution and double aging is used to improve the properties of laser welded joints of K439B alloy. The process of pre-weld and post-weld heat-treatment for solution is: (1160 °C, 4 h, AC), and for double aging is: (1080 °C, 4 h, AC) + (845 °C, 20 h, AC) [13]. The selection of this heat treatment parameter is based on Ref. [11], through which the mechanical properties of the base metal are guaranteed.

To observe the microstructure of the joint, the corrosive agents ($V$(HCl):$V$(H$_2$O$_2$)=9:1) and ($V$(HNO$_3$):$V$(HF):$V$(C$_3$H$_8$O$_3$)=1:2:1) [13] are used for chemical etching to study the morphologies of grains and dendrites and phase distribution. After being etched for 3−5 s, these samples are placed in acetone solution for ultrasonic cleaning. The microstructure and phase distribution of the samples are observed by Olympus BX51M type optical microscope (OM) and Zeiss Sigma 500 type scanning electron microscope (SEM). The types and contents of elements are analyzed by energy-dispersive X-ray spectroscopy (EDS). Based on the randomly selected microstructure images taken by SEM at the same magnification, the quantitative statistics of precipitated phases are carried out by the software Image Pro Plus [10]. For the small $\gamma'$ phase statistics, the whole statistical process is as follows: (1) As carefully as possible, the contrast and brightness of the image are adjusted with a step size of 1/100 so that the particle size is neither expanded nor shrunk. (2) The software (Image Pro Plus) is used to overlay a mask on the image after contrast adjustment to represent the identified particles. The threshold of the mask is

selected from a pixel in the image. Through careful adjustment, the perceived particle size can well reflect the actual size. (3) After the threshold mask is applied, the non-$\gamma'$ phases (such as carbide fragments) in the image are removed, and the contact sites of overlapping particles are manually cut off. The particles at the image boundary will be automatically removed by the software, so the statistics will not be affected. (4) After setting the corresponding ruler, the real size of the particle can be obtained. Then, the number and size of corresponding $\gamma'$ phases are counted. (5) The abnormal data that are too large or too small are removed. The size of the second phase is compared by the equivalent circular diameter transformed from the particle area in the image. In order to reflect the morphological difference, the ratio of the maximum straight line length to the minimum length through the center of the carbide is selected as the evaluation index, which is little affected by the image quality.

The mechanical properties of the joint are characterized by Vickers microhardness and tensile strength at room temperature. The microhardness of the joints is measured by an FM−800 hardness tester made by Future-Tech Company (the load is 500 g, and the holding time is 10 s). Pressure is applied on the centerline of the cross-section of the welding sample, and the indentation spacing is 100 μm. The tensile tests at room temperature are conducted according to ASTM8_E8M20-21 [14].

# 3 Results and discussion

## 3.1 Formation of joints

According to the test criteria in the welding manual, the results of visual observation and weld penetration inspection indicate that there are no surface cracks on the face and back of the five welds, which indicates that the total crack length is 0. The hot cracking sensitivity of K439B welded joint under the experimental parameters is very low. The whole weld is well-formed, and no cracks are observed on the selected metallographic section (Fig. 3(a)). Generally speaking, the hot crack is related to the formation of $\gamma'$ phases and carbides at the grain boundary, and there is much literature on the statistics of weldability of alloy based on the composition of these second phases [26]. The weldability of the alloy can be reflected by the

content of Ti + Al [27] or composition of Al + 0.84%Ti (in wt.%) versus 0.28%Cr + 0.043%Co (in wt.%) to a certain extent [26]. According to the calculation results, K439B is fairly-weldable, which is consistent with the experimental results. On the one hand, the sum of Al and Ti contents of K439B alloy is controlled below 5.5 wt.% (the same composition in most non-weldable alloys is above 6%), and on the other hand, the base metal is treated with solution heat treatment before welding. $\gamma'$ phases are spherical and evenly distributed in the matrix (Fig. 1(c)), indicating that there is a very low lattice mismatch between $\gamma$ and $\gamma'$ phases. A good co-lattice relationship avoids the component liquation under the welding thermal cycle, which is an important factor leading to low crack sensitivity [28]. Actually, there are still a few porosity defects in Fig. 3(a) with maximum size below 48 μm, which were considered acceptable [29].

## 3.2 Microstructure of joint before PWHT

In the base metal, the phase composition of the K439B alloy is analyzed by EDS (Fig. 1(b)). According to the EDS analysis results, there are massive carbides formed by Ti, Nb, Ta, W, and C in the interdendritic regions and at the grain boundaries. A large number of $\gamma'$ phases are simultaneously distributed in the grains and at the grain boundaries. As for welded zone, in Figs. 3(b) and (d), it can be seen clearly that these carbides are mainly distributed between the interdendritic regions. $\gamma'$ phases are mainly distributed around these carbides, which indicates that some elements formed for the carbides and $\gamma'$ phases have unbalanced segregation during the welding process. The phenomenon of massive carbides enveloped by $\gamma'$ phases is also observed in the K447A alloy after solution heat-treatment [22]. The reason is that partial forming elements of carbides such as Ti are also important elements for the formation of the $\gamma'$ phases. No similar phenomenon is observed in the HAZ far away from the weld, where such an obvious segregation does not exist. The study of GU et al [22] shows that the structure is beneficial to relieving the stress concentration around the strip-block carbides and improving the alloy properties. At the same time, there are slight liquation characteristics at the grain boundaries in HAZ (Fig. 3(e)). The eutectic carbides in HAZ are similar in size to those in the weld and much smaller
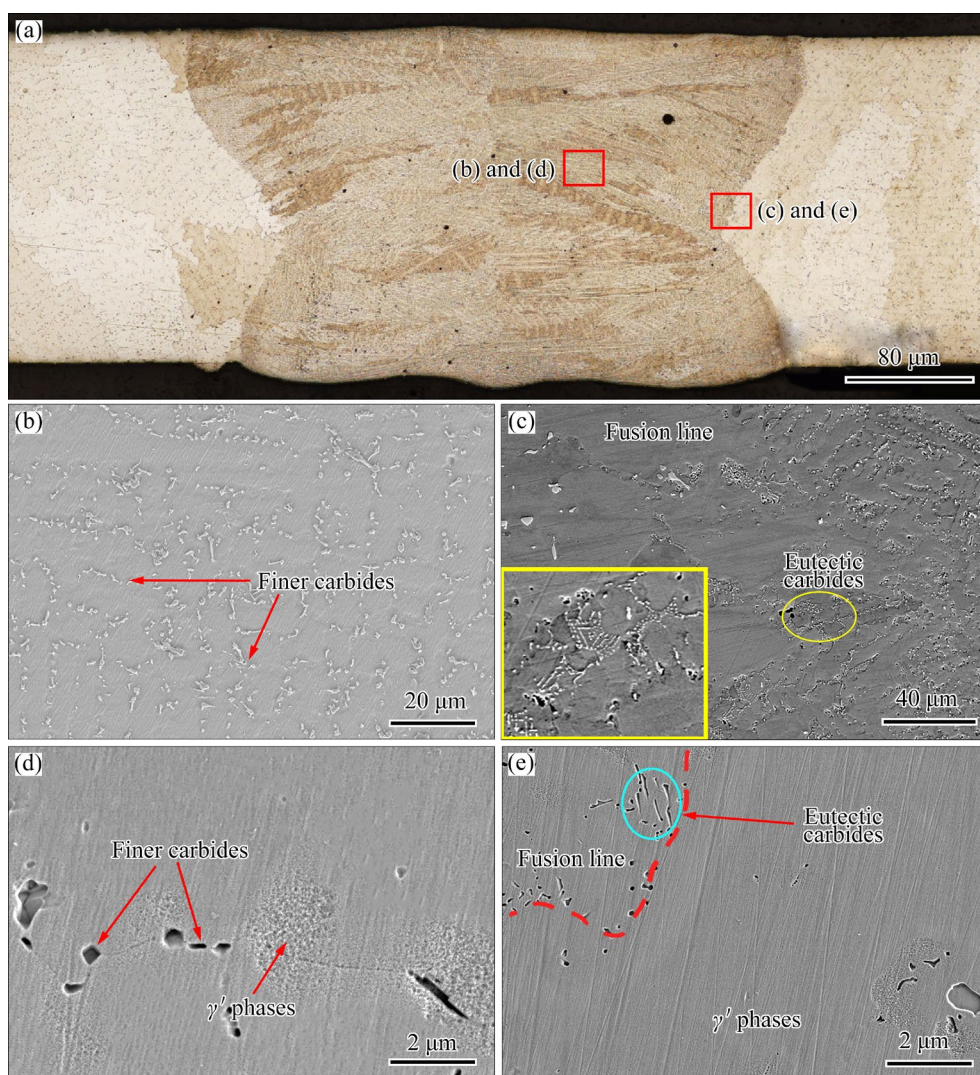
**Fig. 3** Microstructure of joint before PWHT by OM and SEM: (a) Morphology of joint by OM; (b) Carbides in weld by SEM; (c) Carbides in HAZ by SEM; (d) $\gamma'$ phase in weld by SEM; (e) $\gamma'$ phase in HAZ by SEM

than the carbides in base metal. A large number of carbides gather in the same area and cross-link with each other, showing fish-bone shape, which is the characteristic of eutectic carbides. MC-type carbides with eutectic morphology [21] appear near the fusion line, and $\gamma'$ phases are also concentrated around these carbides. In precipitation strengthened nickel-based alloys, the main reason for liquation is penetration mechanism [30], which is caused by the second phase particles (MC carbides, $\gamma'$ phases or eutectic structure, etc.). Under the condition of rapid heating in the welding process, these second phases have not enough time to completely dissolve and undergo eutectic reactions with the matrix, resulting in component liquation, which mainly occurs in precipitation strengthened nickel-based superalloy [31]. The local liquation area of grain

boundary is often concentrated around these eutectic carbides, which indicates that the liquid film of grain boundary is likely caused by the component liquation of MC-type carbides during welding [32]. It is worth mentioning that although local liquation is observed, there is no liquation crack in the joint.

**3.3 Microstructure of joint after PWHT**

The distribution of carbides in the three regions after PWHT is compared by SEM (Figs. 4(a), (b) and (e)). According to Fig. 5 with the distribution of the elements in carbide in the weld before and after heat treatment, the elements in carbide in the weld are still mainly Ti, Ta, Nb and W. Other alloying elements, such as Cr, are almost absent, indicating that the composition of carbides
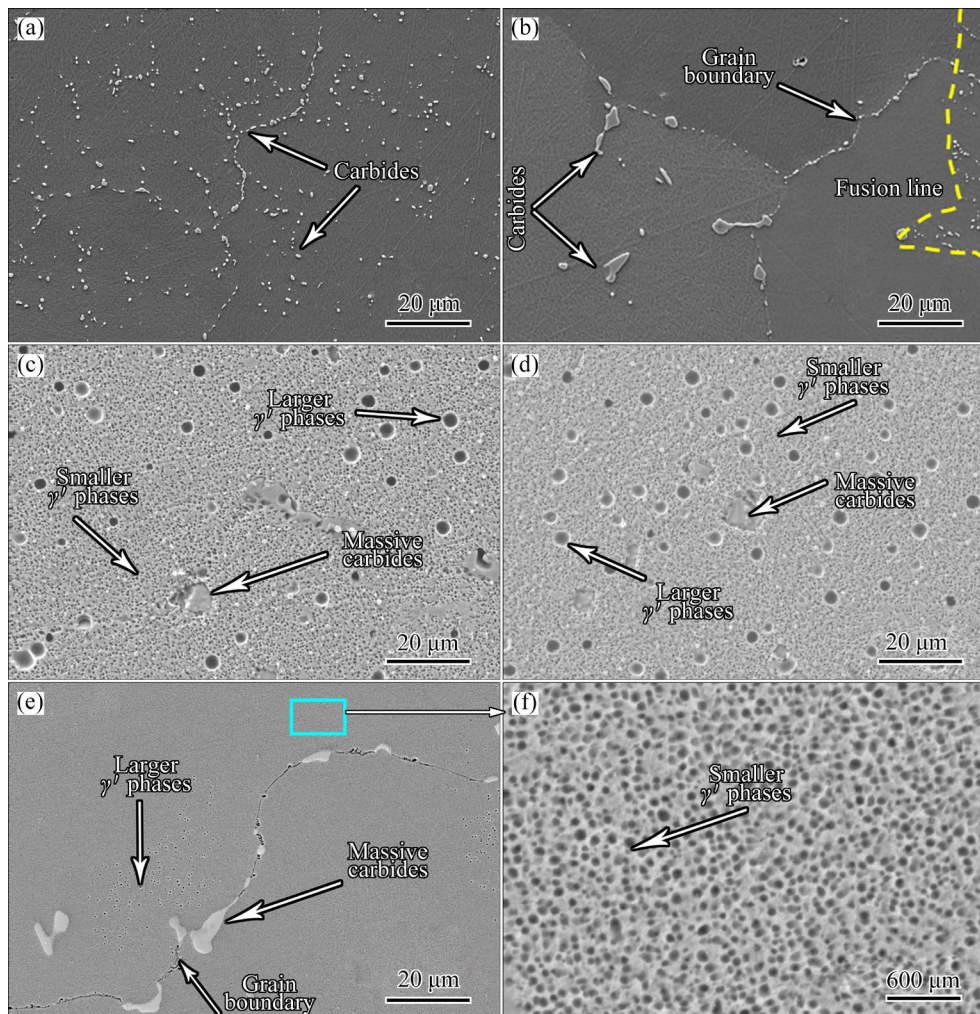
**Fig. 4** Microstructure of joint after PWHT by SEM: (a) Carbides in weld metal zone; (b) Carbides in HAZ; (c) $\gamma'$ phases in weld metal zone; (d) $\gamma'$ phases in HAZ; (e) Carbides in base metal; (f) Local magnification of blue box area in (e)

has not changed significantly. But the morphology, size and distribution of carbides have changed significantly. Based on the SEM images, the quantitative statistics results of carbides and $\gamma'$ phases are shown in Table 2. The results show that after PWHT, the size of carbides in the weld zone grows from 0.161 to 0.378 μm, and the volume fraction increases from 1.78% to 2.25%, while the size of carbides in base metal increases slightly from 1.01 to 1.12 μm, and the volume fraction decreases from 1.29% to 1.15%. One of the most obvious changes is that the volume fraction of spherical carbides (the aspect ratio <2) increases in the weld zone (as shown in Fig. 3(b) and Fig. 4(a)), while the proportion of script-like carbide increases in the base metal zone.

At the larger magnification, the distribution of $\gamma'$ phases is observed by SEM (Figs. 4(c) and (d)).

The statistical results show that before PWHT, the base metal contains about 36.7% spherical $\gamma'$ phase with an average radius of 12.1 nm, while $\gamma'$ phase with a size of about a few nanometers exists only around some carbides in the weld. Its volume fraction is also difficult to calculate; after PWHT, $\gamma'$ phases with two different sizes appear in the whole joint. The average radius of smaller $\gamma'$ and larger $\gamma'$ phases are about 25.7 and 144 nm, respectively. However, different from the larger $\gamma'$ phases distributed uniformly in the weld, the larger $\gamma'$ phases in the base metal are only concentrated around the carbides near the grain boundary.

After the PWHT process of solution, the solute in the joint dissolves and diffuses, and the primary $\gamma'$ phases dissolve in the matrix. Then, the supersaturated solid solution will be obtained. In the first aging stage (high temperature), the fine $\gamma'$
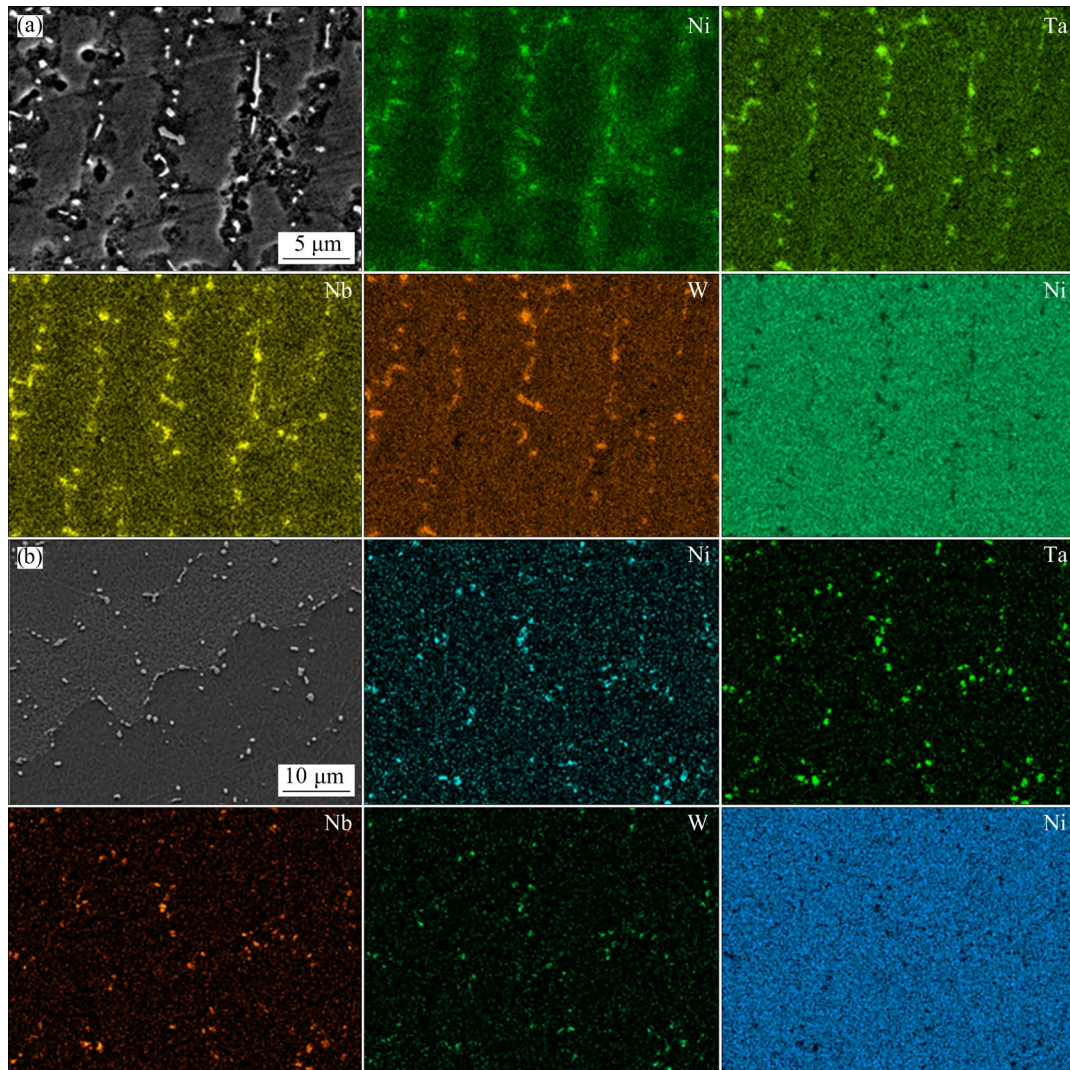
**Fig. 5** EDS results of carbides in weld metal zone: (a) Before PWHT; (b) After PWHT

**Table 2** Quantitative statistics of carbides

| Specimen | Equivalent diameter/μm | Volume fraction/% | Proportion (aspect ratio: 1−2)/% | Proportion (aspect ratio: 2−5)/% | Proportion (aspect ratio: >5)/% |
|---|---|---|---|---|---|
| Weld before PWHT | 0.161 | 1.78 | 61.4 | 35.3 | 3.3 |
| Weld after PWHT | 0.378 | 2.25 | 81.6 | 17.5 | 0.9 |
| Base metal | 1.01 | 1.29 | 59.5 | 37.8 | 2.7 |
| Base metal after PWHT | 1.12 | 1.15 | 18.5 | 66.7 | 14.8 |

The proportions of carbides with different aspect ratios in the table are calculated based on the quantities of carbides

phases will precipitate from the supersaturated solid solution, while in the second aging stage (low temperature), no new $\gamma'$ phases precipitate, but the size and distribution of $\gamma'$ phases will be adjusted to optimize the microstructure and the strength of the joint [33]. The distribution of the bimodal size of the $\gamma'$ phase is due to the coupling effect of the diffusion and the undercooling. According to

Ref. [34], when the spacing between $\gamma'$ phases is smaller than the diffusion distance, nucleation shuts off with soft impingement. At a lower undercooling degree (or higher temperature), the first nucleation occurs. The low driving force and high diffusion coefficient lead to the generation of the primary $\gamma'$ phase. At higher temperature, the nucleation can be shut down (with a higher interparticle distance). As

the temperature drops further, supersaturation increases faster than diffusion depletion. The second nucleation burst occurs, and the secondary $\gamma'$ phase is produced [35,36]. The lower diffusion coefficient at lower temperatures results in the smaller size of the secondary $\gamma'$ phase. Especially, near the grain boundaries, elements tend to segregate and local enrichment often occurs. The consequence of this is that the distribution of the larger $\gamma'$ phases in the base metal is also not uniform, which is mainly concentrated around the carbides near grain boundaries [23,37,38].

### 3.4 Microhardness

A hardness tester was used to measure the microhardness distribution of the as-welded joint. The average microhardness of the base metal zone was HV 418.9, while the lowest hardness of HAZ was only HV 310.4. The average hardness of the weld metal zone was HV 354.3, which was slightly higher than that of HAZ (shown in Fig. 6). The microhardness measured in the sample after PWHT is shown in red line. The microhardness of the joint is improved significantly compared with that before heat-treatment. Especially, in HAZ with low microhardness, the microhardness is increased by about HV 150. The average microhardness of base metal and weld metal zone are both about HV 461.

$\gamma'$ phase can control dislocation movement to strengthen the properties of the alloy [39]. There are two mechanisms of precipitation strengthening: (1) for particles smaller than the critical size, shear mechanism is dominant, including weak coupling dislocation model ($\Delta\tau_{W}$) and strong coupling

dislocation model ($\Delta\tau_{S}$); (2) for particles larger than the critical size, the Orowan looping mechanism ($\Delta\tau_{O}$) plays a major role in strengthening [40]. Based on these shear mechanisms, the critical resolved shear stress can be calculated by the following formulas:

$$\Delta\tau_{W}=\frac{\gamma_{APB}}{2b}\left[\left(\frac{6R\gamma_{APB}f}{\pi T}\right)^{1/2}-f\right] \tag{1}$$

$$\Delta\tau_{S}=\sqrt{1.5}\left(\frac{\mu b}{R}\right)f^{1/2}\frac{\omega}{\pi^{3/2}}\left(\frac{2\pi R\gamma_{APB}}{\omega\mu b^{2}}-1\right)^{1/2} \tag{2}$$

$$\Delta\tau_{O}=\frac{3\mu bf}{4(1-f)R} \tag{3}$$

where the antiphase boundary energy $\gamma_{APB}=0.12$ J/m$^2$, $R$ is the radius of $\gamma'$ phases, $f$ is the volume fraction of $\gamma'$ phases, $b$ is the amplitude of Burgers vector of $a/2\langle110\rangle$ (generally, $b=0.25$ nm), $T$ is the line tension of the dislocations, $T=1/(2\mu b^2)$, $\mu$ is the shear modulus ($\mu=60$ GPa), and $\omega$ (=1) is a dimensionless constant [40].

Based on the statistical results of $\gamma'$ phases in the weld and base metal before and after heat treatment, the corresponding shear stress is calculated and shown in Table 3. In the weld zone, the strengthening mechanism dominated by small $\gamma'$ phases is strong coupling dislocation model, $\Delta\tau_{S}$ is less than 4.8 MPa, while the base metal is dominated by weak coupling dislocation model, where the stress reaches 63.8 MPa. Therefore, the contribution of $\gamma'$ phase to the hardness improvement in the base metal is much higher than that in the weld. After
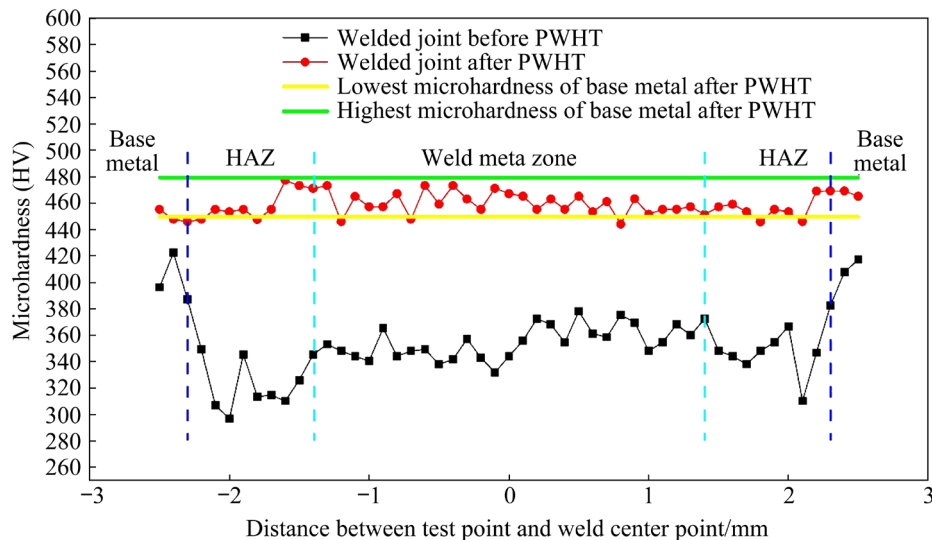


**Fig. 6** Comparison of microhardness distribution of samples before and after PWHT

heat treatment, the radius and volume fraction of the small $\gamma'$ phases in the weld zone reach 25.7 nm and 28.2%, respectively, which are very close to those of the base metal. The strengthening mechanism is the strong coupling dislocation model, and $\Delta\tau_W$ reaches 92.0 and 102.4 MPa, respectively. Moreover, considering the large amount of fine granular carbides in the weld zone after heat treatment [19], the hardness of the whole joint is evenly distributed.

### 3.5 Tensile properties

At room temperature, tensile tests are carried out for the base metal and welding samples after PWHT. Ultimate Tensile strength, yield strength and elongation are measured to obtain the tensile performance. Fracture condition of the specimens is shown in Fig. 7(a). The welded samples are fractured on the base metal, which indicates that the ultimate tensile strength of the joint at room temperature is equal to that of the base metal. As can be seen from Fig. 7(b), the ultimate tensile strength and yield strength of the welded samples are 1075.5 and 799.1 MPa, which are consistent with those of the base metal (Fig. 7(b)), but the elongation slightly decreases from 8.2% to 7.6% compared with the base metal (Fig. 7(b)). Large MC-type carbides have an adverse effect on tensile properties [21,41]. LIANG et al [42] interprets the influence of script-type carbides on the properties, and finds that carbides with longer arm length and narrower cross-section width have more obvious cracking tendency through the calculation of Griffith cracking theoretical model, while spherical carbides have good cracking resistance. As mentioned in the previous quantitative statistics of carbides, there are more script-like carbides in the base metal after heat treatment, which becomes the reason for the preferential cracking in the base metal zone during the tensile process. Compared to the base metal, the inhomogeneity of the joints results in a certain decrease in elongation.

Figure 8 shows the fracture surface and cross-section of the specimens. The broken carbides and dimples can be seen on the fracture surface. The existence of dimples is a typical characteristic of ductile fracture. It is observed that the cracks that appear after stretching are concentrated at the grain boundary. The carbides fractured at the grain boundary are also visible, which is consistent with

**Table 3** Quantitative statistics of $\gamma'$ phases and calculation of critical resolved shear stress

| Specimen | Radius of $\gamma'$ phase/nm | Volume fraction of $\gamma'$ phase/% | $\Delta\tau_W$/MPa | $\Delta\tau_S$/MPa | $\Delta\tau_O$/MPa |
|---|---|---|---|---|---|
| Weld | <5 | <3 | 16.4 | <4.8 | 22.7 |
| Weld after PWHT | 25.7 | 28.2 | 92.0 | 139.2 | 171.9 |
| Base metal | 12.1 | 36.7 | 63.8 | 153.1 | 228.3 |
| Base metal after PWHT | 28.9 | 29.2 | 102.4 | 135.2 | 160.3 |

The size of $\gamma'$ phase in the weld zone is small and difficult to calculate. The actual shear stress will be smaller than the calculated value, but this will not affect the conclusion
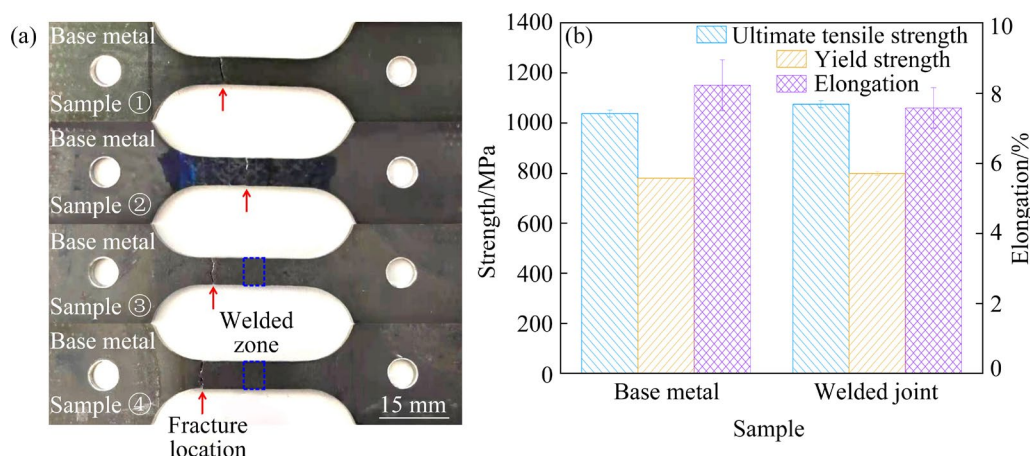


**Fig. 7** Room temperature tensile results of joint before and after PWHT: (a) Fracture location (as indicated by red arrow); (b) Tensile properties of samples
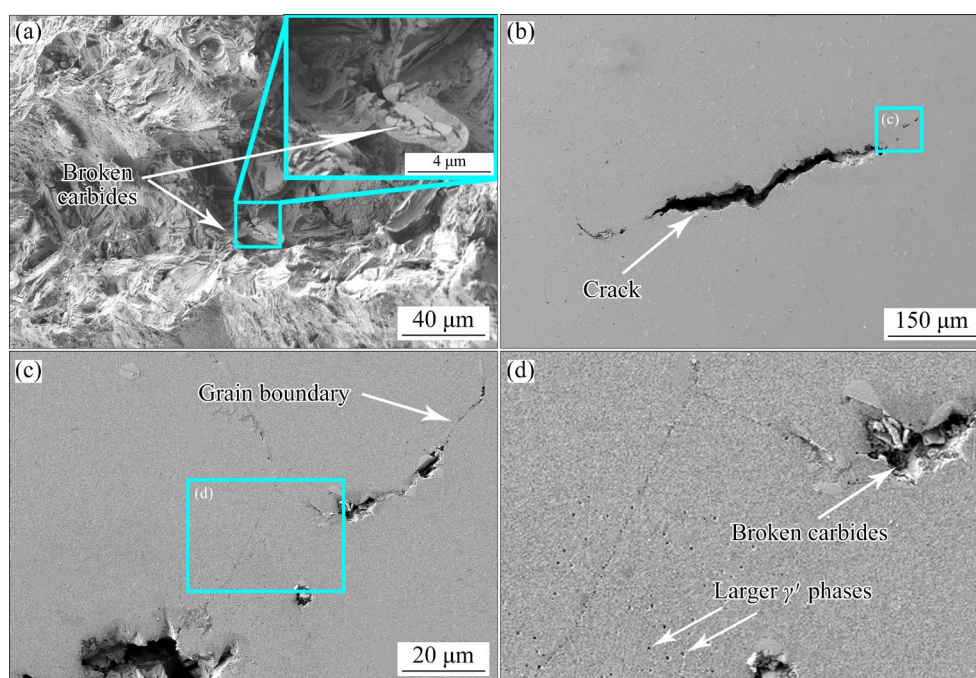
**Fig. 8** Morphology of tensile fracture surface and cross-section: (a) Broken carbides on fracture surface and small shallow dimples; (b) Crack near fracture surface; (c) One of sources of crack germination; (d) Broken carbides and larger $\gamma'$ phases near crack

the results observed in the fracture morphology. The whole tensile fracture process of the samples at room temperature is summarized as follows: the larger size $\gamma'$ phases are concentrated at the grain boundaries of base metal, which results in their lower strength and larger deformation. Meanwhile, a large number of hard and brittle carbides are distributed at the grain boundaries. In the process of stretching at room temperature, due to the stress concentration around the carbides, part of the carbides at the grain boundaries break first and become the micro-crack sources. The micro-cracks spread along the grain boundaries with low strength and finally break. Combined with the fracture morphology, it is inferred that the crack source is initiated at the carbides at the grain boundary with weak strength, and then extends into the grain near the larger $\gamma'$ phases because of the severer plastic deformation.

## 4 Conclusions

(1) The new nickel-based alloy K439B has low crack sensitivity. The quantitative statistic results of $\gamma'$ phase and carbide show that the $\gamma'$ phases in the weld zone are tiny and even negligible due to the

high heating and cooling rates of laser welding. The $\gamma'$ phases are concentrated around carbides at the grain boundary due to the segregation and enrichment of elements.

(2) After PWHT, the distributions of carbides and $\gamma'$ phases are improved. $\gamma'$ phases are distributed uniformly in two sizes in the weld and HAZ. At the same time, new finer granular carbides appear at the grain boundary in base metal and HAZ. The number of spherical carbides increases in the weld zone. The proportion of carbides with aspect ratio less than 2 increases from 61.4% to 81.6% due to segregation being resolved after PWHT.

(3) Based on the theoretical calculation of the strengthening mechanism of $\gamma'$ phase, the strengthening effect of $\gamma'$ phases in the weld is dominated by the strong coupling dislocation mechanism, and $\Delta\tau_S$ is lower than 4.8 MPa. After PWHT, the size of $\gamma'$ phase increases to 25.7 nm, the weak coupling dislocation mechanism dominates the strengthening effect, and $\Delta\tau_W$ reaches 92.0 MPa. It explains the obvious increase of microhardness in the joint after heat treatment.

(4) The ultimate tensile strength and yield strength of the joint after heat treatment reach 1075.5 and 799.1 MPa, respectively, which are

similar to those of the base metal after PWHT. The script-like carbides in the base metal become the fracture source during the tensile process. The larger $\gamma'$ phase (about 150 nm in radius) is localized at the grain boundary in the base metal, which further promotes the preferential fracture of the base metal in the joint during the tensile process.

## CRediT authorship contribution statement

**Zheng LI:** Conceptualization, Formal analysis, Writing − Original draft, Writing − Review and editing, Investigation, Data curation; **Zhen-lin ZHANG:** Methodology, Writing − Original draft; **Ai-ping WU:** Writing − Review and editing, Investigation, Supervision; **Ming-jun ZHANG:** Resources, Investigation; **Ju KANG:** Resources; **Qu LIU:** Visualization; **Zhao YUE:** Conceptualization, Writing − Review and editing, Resources, Supervision, Project administration, Funding acquisition; **Jing-yang CHEN:** Writing − Review and editing, Project administration, Funding acquisition.

## Declaration of competing interest

The authors declare that they have no known competing financial interests or personal relationships that could have appeared to influence the work reported in this paper.

## References

[1]     ZHANG Ming-jun, ZHANG Lei-lei, HU Ying-tao, TANG Xin, YANG Qing. Effect of hot isostatic pressing on microstructure of K439B superalloy [J]. Heat Treatment of Metals, 2020, 45(11): 177−181. (in Chinese)

[2]     CHOUDHURY B, CHANDRASEKARAN M. Investigation on welding characteristics of aerospace materials—A review [J]. Materials Today: Proceedings, 2017, 4(8): 7519−7526.

[3]     QU Feng-sheng, LIU Xu-guang, XING Fei, ZHANG Kai-feng. High temperature tensile properties of laser butt-welded plate of Inconel 718 superalloy with ultra-fine grains [J]. Transactions of Nonferrous Metals Society of China, 2012, 22(10): 2379−2388.

[4]     ZHANG Zhen-lin, ZHAO Yue, SHAN Ji-guo, WU Ai-ping, SATO Y S, TOKITA S, KADOI K, INOUE H, GU Huai-peng, TANG Xin. The role of shot peening on liquation cracking in laser cladding of K447A nickel superalloy powders over its non-weldable cast structure [J]. Materials Science and Engineering: A, 2021, 823: 141678.

[5]     ZHANG Zhen-lin, ZHAO Yue, SHAN Ji-guo, WU Ai-ping, SATO Y S, TOKITA S, KADOI K, INOUE H, GU Huai-peng, TANG Xin. Evolution behavior of liquid film in the heat-affected zone of laser cladding non-weldable nickel-based superalloy [J]. Journal of Alloys and Compounds, 2021, 863: 158463.

[6]     ZHANG Zhen-lin, ZHAO Yue, CHEN Yang, SU Zhen, SHAN Ji-guo, WU Ai-ping, SATO Y S, GU Huai-peng, TANG Xin. The role of the pulsed-wave laser characteristics on restraining hot cracking in laser cladding non-weldable nickel-based superalloy [J]. Materials & Design, 2021, 198: 109346.

[7]     LONG Yi-tong, NIE Pu-lin, LI Zhu-guo, HUANG Jian, LI Xiang, XU Xi-mei. Segregation of niobium in laser cladding Inconel 718 superalloy [J]. Transactions of Nonferrous Metals Society of China, 2016, 26(2): 431−436.

[8]     CHANDRAN M, SONDHI S K. First-principle calculation of APB energy in Ni-based binary and ternary alloys [J]. Modelling and Simulation in Materials Science and Engineering, 2011, 19(2): 025008.

[9]     RAYNOR D, SILCOCK J M. Strengthening mechanisms in $\gamma'$ precipitating alloys [J]. Metal Science Journal, 1970, 4(1): 121−130.

[10]   HAWK J A, CHENG Tian-le, SEARS J S, JABLONSKI P D, WEN You-hai. Gamma prime stability in Haynes 282: Theoretical and experimental considerations [J]. Journal of Materials Engineering and Performance, 2015, 24(11): 4171−4181.

[11]   LIU Gang, KONG Ling-bing, XIAO Xue-shan, BIROSCA S. Microstructure evolution and phase transformation in a nickel-based superalloy with varying Ti/Al ratios: Part 1—Microstructure evolution [J]. Materials Science and Engineering: A, 2022, 831: 142228.

[12]   KAZEMPOUR-LIASI H, TAJALLY M, ABDOLLAH-POUR H. Liquation cracking in the heat-affected zone of IN939 superalloy tungsten inert gas weldments [J]. International Journal of Minerals, Metallurgy and Materials, 2020, 27(6): 764−773.

[13]   ZHANG Lei-lei, CHEN Jing-yang, QIAN Lei, ZHANG Ming-jun, TANG Xin, YANG Qing. Effect of casting temperature on microstructure and mechanical properties of K439B superalloy [J]. Transactions of Materials and Heat Treatment, 2019, 40(9): 57−63. (in Chinese)

[14]   LIM L C, LIU N, YI J Z, MA Q. Cyclic overaging pre-weld heat treatment of Rene 80: Effect of solution treatment and end aging temperatures [J]. Materials Science and Technology, 2002, 18(4): 420−428.

[15]   GAO Shuang, SONG Zhen-feng, HE Bo, ZHOU Lan-zhang, HOU Jie-shan. Effect of Ta addition on solidification microstructure and element segregation of IN617B nickel-base superalloy [J]. Transactions of Nonferrous Metals Society of China, 2022, 32(2): 559−568.

[16]   SAFARAZADE A, SHARIFITABAR M, AFARANI M S. Effects of heat treatment on microstructure and mechanical properties of Inconel 625 alloy fabricated by wire arc additive manufacturing process [J]. Transactions of Nonferrous Metals Society of China, 2020, 30(11): 3016−3030.

[17]   REZAEI M A, NAFFAKH-MOOSAVY H. The effect of

pre-cold treatment on microstructure, weldability and mechanical properties in laser welding of superalloys [J]. Journal of Manufacturing Processes, 2018, 34: 339−348.

[18] CHEN Z Y, TAHERI M. The effect of pre-heating and pre-cold treatment on the formation of liquation and solidification cracks of nickel-based superalloy welded by laser beam [J]. Journal of Materials Research and Technology, 2020, 9(5): 11162−11177.

[19] ALBARRAN G M A, MARTINEZ D I, DIAZ E, DIAZ J C, GUZMAN I, SAUCEDO E, GUZMAN A M. Effect of preweld heat treatment on the microstructure of heat-affected zone (HAZ) and weldability of Inconel 939 superalloy [J]. Journal of Materials Engineering and Performance, 2014, 23(4): 1125−1130.

[20] TAHERI M, HALVAEE A, KASHANI-BOZORG S F. Effect of pre- and post-weld heat treatment on microstructure and mechanical properties of GTD-111 superalloy welds [J]. Metals and Materials International, 2021, 27(5): 1173−1192.

[21] XIE Ji-lin, MA Ying-che, XING Wei-wei, OU Mei-qiong, ZHANG Long, LIU Kui. Microstructure and mechanical properties of a new cast nickel-based superalloy K4750 joint produced by gas tungsten arc welding process [J]. Journal of Materials Science, 2019, 54(4): 3558−3571.

[22] GU Huai-peng, LI Xiang-hui, GAI Qi-dong, TANG Xin. Study on the heat-treated microstructure and tensile property of K447A alloy [J]. Foundry, 2014, 63(8): 824−827.

[23] ZHANG Ming-jun, JIANG Hua, KONG Jin-ling, CHEN Jing-yang, TANG Xin, XIAO Cheng-bo. Effects of HIP temperature on microstructure and high temperature mechanical properties of K438 alloy [J]. Transactions of Materials and Heat Treatment, 2015, 36(12): 98−102. (in Chinese)

[24] Chinese Welding Society. Manual welding [M]. 3rd ed. Beijing: China Machine Press, 2007. (in Chinese)

[25] SHAO Ying-kai, WANG Yu-xi, YANG Zhi-bin, SHI Chun-yuan. Plasma-MIG hybrid welding hot cracking susceptibility of 7075 aluminum alloy based on optimum of weld penetration [J]. Acta Metallurgica Sinica, 2018, 54(4): 547−556.

[26] ACHARYA R, DAS S. Additive manufacturing of IN100 superalloy through scanning laser epitaxy for turbine engine hot-section component repair: Process development, modeling, microstructural characterization, and process control [J]. Metallurgical and Materials Transactions A, 2015, 46(9): 3864−3875.

[27] MASHHURIAZAR A, OMIDVAR H, SAJURI Z, GUR C H, BAGHDADI A H. Effects of pre-weld heat treatment and heat input on metallurgical and mechanical behaviour in HAZ of multi-pass welded IN-939 superalloy [J]. Metals, 2020, 10(11): 1453.

[28] LACHOWICZ M, DUDZINSKI W, PODREZ- RADZIS-ZEWSKA M. TEM observation of the heat-affected zone in electron beam welded superalloy Inconel 713C [J]. Materials Characterization, 2008, 59(5): 560−566.

[29] HU Xiao-an, XUE Zhi-yuan, ZHAO Gao-le, YUN Jiang, SHI Duo-qi, YANG Xiao-guang. Laser welding of a selective laser melted Ni-base superalloy: Microstructure and high temperature mechanical property [J]. Materials Science and Engineering: A, 2019, 745: 335−345.

[30] OJO O A, CHATURVEDI M C. On the role of liquated $\gamma'$ precipitates in weld heat affected zone microfissuring of a nickel-based superalloy [J]. Materials Science and Engineering: A, 2005, 403(1): 77−86.

[31] CAO X, RIVAUX B, JAHAZI M, CUDDY J, BIRUR A. Effect of pre- and post-weld heat treatment on metallurgical and tensile properties of Inconel 718 alloy butt joints welded using 4 kW Nd:YAG laser [J]. Journal of Materials Science, 2009, 44(17): 4557−4571.

[32] GONZALEZ M A, MARTINEZ D I, PEREZ A, GUAJARDO H, GARZA A. Microstructural response to heat affected zone cracking of prewelding heat-treated Inconel 939 superalloy [J]. Materials Characterization, 2011, 62(12): 1116−1123.

[33] ZHANG Zhen-lin, ZHAO Yue, SHAN Ji-guo, WU Ai-ping, GU Huai-peng, TANG Xin. Influence of heat treatment on microstructures and mechanical properties of K447A cladding layers obtained by laser solid forming [J]. Journal of Alloys and Compounds, 2019, 790: 703−715.

[34] WEN Y H, SIMMONS J P, SHEN C, WOODWARD C, WANG Y. Phase-field modeling of bimodal particle size distributions during continuous cooling [J]. Acta Materialia, 2003, 51(4): 1123−1132.

[35] CHONG Yan, LIU Zheng-dong, GODFREY A, WANG Lu, LIU Wei, WENG Yu-qing. Heat treatment of a candidate material for 700 °C A-USC power plants [J]. Journal of Iron and Steel Research International, 2015, 22(2): 150−156.

[36] HWANG J Y, NAG S, SINGH A R P, SRINIVASAN R, TILEY J, FRASER H L, BANERJEE R. Evolution of the $\gamma/\gamma'$ interface width in a commercial nickel base superalloy studied by three-dimensional atom probe tomography [J]. Scripta Materialia, 2009, 61(1): 92−95.

[37] ZHONG Zhi-yong, LIU Jian-tao, ZHANG Yi-wen, LI Xiao-kun, JIA Jian. Effect of solution and aging temperature on microstructure and properties of a new powder superalloy [J]. Powder Metallurgy Industry, 2021, 31(1): 56−63. (in Chinese)

[38] ATABAY S E, SANCHEZ-MATA O, MUNIZ-LERMA J A, BROCHU M. Microstructure and mechanical properties of difficult to weld Rene 77 superalloy produced by laser powder bed fusion [J]. Materials Science and Engineering: A, 2021, 827: 142053.

[39] KAYACAN R, VAROL R, KIMILLI O. The effects of pre- and post-weld heat treatment variables on the strain-age cracking in welded Rene 41 components [J]. Materials Research Bulletin, 2004, 39(14/15): 2171−2186.

[40] XU Ya-xin, LI Wen-ya, YANG Xia-wei, GU Yue-feng. Evolution of grain structure, $\gamma'$ precipitate and hardness in friction welding and post weld heat treatment of a new Ni−Fe based superalloy [J]. Materials Science and Engineering: A, 2020, 788: 139596.

[41] ZHANG Gui-ju, XIAO Cai-yuan, TAHERI M. Effect of Nd:YAG pulsed laser welding process on the liquation and strain-age cracking in GTD-111 superalloy [J]. Journal of Manufacturing Processes, 2020, 52: 66−78.

[42] LIANG Tao-sha, WANG Lei, LIU Yang, SONG Xiu. Role of script MC carbides on the tensile behavior of laser-welded fusion zone in DZ125L/IN718 joints at 650 °C [J]. Journal of Materials Science, 2020, 55(27): 13389−13397.

# 激光焊接及焊后热处理 K439B 合金的显微组织与力学性能

李 郑 [1,2]，张振林 [3]，吴爱萍 [1,2,4]，张明军 [5]，康 举 [6]，刘 瞿 [1,2]，赵 玥 [1,2]，陈晶阳 [5]

1. 清华大学 机械工程系，北京 100084；
2. 清华大学 先进材料加工技术教育部重点实验室，北京 100084；
3. 西南交通大学 材料科学与工程学院，成都 610031；
4. 清华大学 摩擦学国家重点实验室，北京 100084；
5. 北京航空材料研究院 先进高温结构材料重点实验室，北京 100095；
6. 北京石油化工学院 北京能源工程先进连接技术高等学校工程研究中心，北京 102617

**摘 要：** 对应用于发动机涡轮上的新型镍基合金 K439B 进行激光焊接实验，研究焊后热处理对接头显微组织和力学性能的影响。半定量分析结果表明，热处理后接头各区域 $\gamma'$ 相均发生长大，一次 $\gamma'$ 相和二次 $\gamma'$ 相半径分别约为 25 和 150 nm。力学性能测试结果表明，焊后热处理可使焊缝区硬度提高约 HV 100，由 $\gamma'$ 相提供的临界恢复剪应力从 4.8 MPa 提高到 92 MPa；另一方面，热处理后接头的抗拉强度和屈服强度与母材的相当，大量碳化物的存在导致接头在拉伸过程中优先断裂于母材处。

**关键词：** 镍基高温合金；激光焊接；$\gamma'$ 相；碳化物；显微组织；力学性能

**(Edited by Wei-ping CHEN)**